PRZEGLĄD ELEKTROTECHNICZNY

Ukazuje się od 1919 roku 2'2024

Organ Stowarzyszenia Elektryków Polskich • Wydawnictwo SIGMA-NOT Sp. z o.o.

1. Abdalrhman Adel[1], 2. Osama A. Omer [1], 3. M. Alamir[2], 4. M. Anwar[3], 5. C. Qunsheng[4], 6. Amir Almslmany[5]

Dept. of Electronics & Communication Faculty of engineering, Aswan University (1), Dept. of Electronics &Communication, Alexandria Higher Institute (2), Faculty of Science, Aswan University (3), Dept. of Electronic Science and Technology, Nanjing University of Aeronautics & Astronautics (4), Dept. of Electronics & Communication, Air Defense College (5)
ORCID: 6. https://orcid.org/0000-0002-8271-9734

doi:10.15199/48.2024.02.01

A Unique Optical System Design and Implementation of X- Ray system to Non-destructive Tests Solid Fuel missiles

Abstract. *One of the most important military applications in missile science is the careful X-ray examination (XRE) of solid rocket fuel samples. So that it becomes clear whether the missile fuel is made efficiently and achieves its goal or not, which is a regular combustion rate from the moment of launch to the end of its flight. The main dependency of this is to provide expenses for the real launch of missiles to ensure the work of the solid fuel that has been manufactured. In this paper, we review a visual diagnostic system with X-rays for solid fuel samples (SFS) before starting the field tests to detect manufacturing defects. An optimal design of the X-ray device was made in terms of transmission and the radiation collection system to focus it on the sample to be tested and to choose the most appropriate X-ray detector for this purpose. The metal casing of the X-ray tube (XRT), the collimator, and the mechanical equipment of the entire system were also designed and implemented, with the assembly of parts and components of the X-ray camera. The system was tested on two real samples. The first is made efficiently and does not have any manufacturing defects, while the other has air bubbles. The proposed system succeeded in giving accurate images for both samples. This made evaluating fuel performance possible without costly field experiments.*

Streszczenie. *Jednym z najważniejszych zastosowań wojskowych w nauce o rakietach jest dokładne badanie rentgenowskie (XRE) próbek stałego paliwa rakietowego. Żeby było jasne, czy paliwo rakietowe jest produkowane wydajnie i osiąga swój cel, czyli równomierne spalanie od chwili wystrzelenia do końca lotu. Główną zależnością jest zapewnienie wydatków na rzeczywiste wystrzelenie rakiet, aby zapewnić pracę wyprodukowanego paliwa stałego. W tym artykule dokonujemy przeglądu wizualnego systemu diagnostyki za pomocą promieni rentgenowskich próbek paliwa stałego (SFS) przed rozpoczęciem testów terenowych w celu wykrycia wad produkcyjnych. Wykonano optymalną konstrukcję urządzenia rentgenowskiego pod względem transmisji oraz układu odbioru promieniowania, aby skupić je na badanej próbce i wybrać najwłaściwszy do tego celu detektor promieniowania rentgenowskiego. Zaprojektowano i wdrożono także metalową obudowę lampy rentgenowskiej (XRT), kolimator oraz wyposażenie mechaniczne całego układu, wraz z montażem części i podzespołów kamery rentgenowskiej. System został przetestowany na dwóch rzeczywistych próbkach. Pierwsza jest wykonana sprawnie i nie posiada wad produkcyjnych, natomiast druga posiada pęcherzyki powietrza. Zaproponowany system pozwolił uzyskać dokładne obrazy obu próbek. Umożliwiło to ocenę wydajności paliwa bez kosztownych eksperymentów w terenie. (**Projekt unikalnego systemu optycznego i wdrożenie systemu rentgenowskiego do badań nieniszczących rakiet na paliwo stałe**)*

Keywords: X-ray examination (XRE); solid fuel samples (SFS); and X-ray tube (XRT).
Słowa kluczowe: Badanie rentgenowskie (XRE); próbki paliwa stałego (SFS); i lampa rentgenowska (XRT).

Introduction

Rontgen discovered X-rays in 1895, and the first von Laue-proposed diffraction experiments carried out in 1913 proved that they are waves [1]. Later investigations demonstrated that X-rays are electromagnetic waves and transverse waves. The minimum wavelength for gamma rays is 0.1A, whereas the highest wavelength for X-rays is A 100. (Which is the maximum for ultraviolet waves). This range corresponds to the 0.1 to 100 Key energy range [2]. An electron accelerated in an electric field collides with the anode, a target built of metallic material, to produce X-rays. The radiant energy is only a part of the energy of the accelerating electron. Thus, it worked to establish a quantity known as the X-ray generation efficiency ɳ [3].in equation 1 show the relation between the energy of photon and electron.

$$(1)\quad \frac{photon\ energy}{elctron\ energy} = \eta = 1.1 \times 10^{-9} z.v$$

Where Z is Atomic number and V is the electric potential used to accelerate the electrons in (see Fig.1) the general configuration of x-ray tube. The x-ray tube consists of some main components, cathode, anode and the body of tube and high voltage power supply.

Due to the high transmittance of X-rays, they are used in diagnostic applications for both medical and industrial applications [4]. One of the most important industrial uses of X-rays is the non-destructive testing of products. To detect manufacturing defects, this function is very important in the quality department, but it provides a lot of necessary information about manufacturing quality and detecting unwanted defects [5].Solid fuel research has been a focus area of the Propulsion Research Centre (PRC) at the University of Alabama in Huntsville (UAH) for more than 20 years [6]. Previous projects have looked at a variety of research topics related to solid fuels.

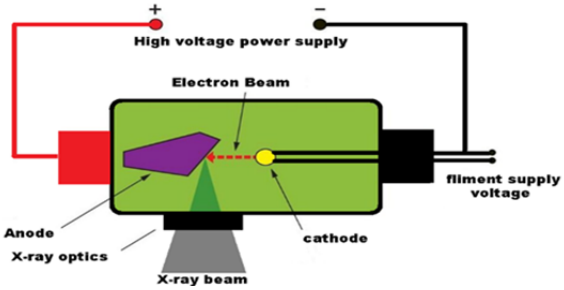

Fig.1. General Form of x-ray tube.

Including the combustion rate measurement of current or projected solid fuel technologies [7], Optimization of measurement methods as well as research on composition and inert mixing. In previous studies, combustion rate estimation techniques have used timing wires, implanted thermocouples [8].

Real-time x-ray radiography system and transducers. X-ray source, detector, computer and software off-the-shelf products (COTS) used in post-processing [9]. Real-time X-ray radio fluoroscopy for solid-state combustion evaluation in two dimensions Motivate content by time. Although solid fuels can be measured in several ways Most of these combustion rate explanatory methods are based on measurements that take ambient air away from the surface of the burning solid fuel [10]. Estimates and derived curves for the combustion rate although the procedures are often very accurate, they do not provide a direct way to see or measure the total surface area of a smouldering pulse. For solids, the X-ray measurement technique is very useful. Since the combustion surface of the fuel can be imagined, sometimes complex or unusual fuel engineering is used [11]. Conventional solid fuel consists of a mixture of an oxidant in the solid state. The solid body of the solid fuel is the grains of aluminium with some other components of the solid fuel. The rate of burning is known as the grain gradient rate and is usually represented in cm/sec, mm/sec or inch/sec. Solid fuel granules are calculated by the combustion surface [12].

Basically, perpendicular to the surface in this direction. To ensure accurate measurements are made constant distance is created between adjacent surface lines while drawing successive charred surfaces [13]. The composition of the propellant affects the typical solid fuel combustion rate [14]. This paper is organized as follows. Section 2 techniques of the modern x-ray systems, section 3 types of x-ray detection sensors, section 4 optical proposed system design and section 5 results and section 6 conclusions.

Techniques of the Modern X-Ray Systems

In X-ray detection techniques, there are two systems for detection. The first is the conical projection system, and this system gives a two-dimensional image, among its most prominent defects is the difficulty of analysing the image clearly, especially in industrial applications, like detecting internal defects of the crystal formation in solid fuel columns of missiles engine [14]. (See Fig. 2) principle the conical projection system.

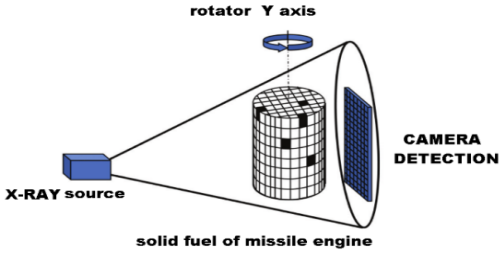

Fig. 2. Principle the conical projection system.

In this Figure, X-rays are sent from the valve in the direction of the sample to be examined, from columns of solid rocket fuel, and then the X-rays pass through the column of solid fuel and give a two-dimensional image of the solid fuel. Then to the opposite direction, as the work of the sample is prepared on the axis of rotation to photograph the entire sample, to perform the accurate analysis of that sample. This technique is difficult to use with large volume samples of solid rocket fuel plumes. This requires, if used for analysis, large-sized mechanical equipment with a number of x-ray producing valves and a number of cameras to take a picture of those rays after they pass through the sample. The second technique is the 3D computed tomography technique, this technique relies on an X-ray transmitter and a set of detection cameras for receiving transient rays from the sample, the transmitter and receiver are placed on a rotating axis that wraps around the entire sample to enable it to take an accurate analytical image of the sample to be examined [15]. (See Fig. 3) the working theory of X-ray computed tomography.

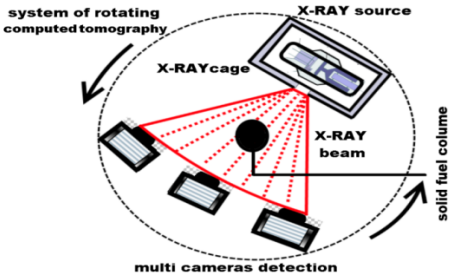

Fig. 3. The working theory of X-ray computed tomography.

This technology is considered one of the most important technologies currently used in medical and industrial applications, especially the application of detecting manufacturing defects for solid missile fuel systems. But at the same time, it is complex. And it requires a very accurate synchronization in the working system between the cameras that detect the X-rays passing through the sample to be photographed. Also, the entire system operates on a rotating axis and the sample is fixed, which makes the work method more complex than the previous technology and costlier.

Types of X-Ray Detection Sensors

The interaction of the X-ray photons with the molecules of the sample to be imaged is detected by the sensitive site detector. This detector has undergone extensive development over the past few decades. Radiation detection applications are widely used today such as medical and industrial applications. By using pixel detectors, which is an array of a large number of detectors, which work to form an image with precise specifications, the image formed is as a result of the diffraction of X-rays in the crystals and particles of the sample to be imaged, when the rays hit the sensor matrix, a two- or three-dimensional image can be formed, depending on the technological application and its purpose [16]. The following are the most important modern detection systems in the field of X-ray imaging to find out the specifications of the detector to be designed for the proposed system.

Monolithic Active Pixel Sensor (MAPS)

Silicon diodes and a readout circuit are coupled to create monolithic active pixel sensors (MAPS). It has been shown to be a promising technique for high-resolution X-ray detectors since it can be manufactured using conventional CMOS technology and in the same pixel units. In addition it produces very precise individual pixel readouts while running at high speeds with low power consumption, from a single, low voltage source, and is inexpensively constructed, even in huge matrix sizes, and compact to demands. Close contact with the sensor results in reduced ground noise and successful operation with a sense of the smallest X-ray signals with a high S/N ratio without the need for extra electrical amplifiers. The effectiveness and speed of all freed charge carriers in the reactions inside the MAPS type detector, enabling the sensor to give an accurate picture of the sample to be visualized analysis. Mixed pixel detectors have a sensor interface that is adjustable in size

in terms of the number of detectors. While the thickness of the active element in MAPS depends on the substrate used in the CMOS technology Sensor size can be changed depending on the application [17]. (See Fig. 4) 3D designs of maps image detector array internal cage limiters made from metal lead system.

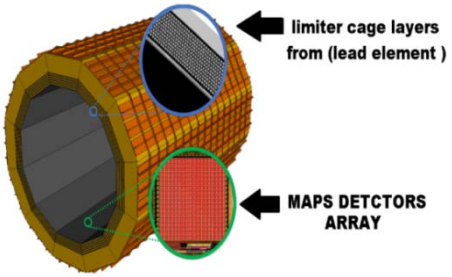

Fig. 4. 3D design of MAPS image detector array internal cage limiters made from Metal lead system.

In that Fig, the installation of a maps imaging detector, used in industrial applications for detection of manufacturing defects and non-destructive testing of products, is shown. This sensor consists of a cylindrical shape made of layers of lead that are impermeable to X-rays and in a crystal form that reflects the rays when they enter the supernova so that a concentration of X-rays occurs on the inner wall of the sensor, which contains a number of maps arrays, which helps in not losing radiation falling on the sensor by a large percentage. Important note: This sensor has a response speed of microseconds, it gives a good quality image, but it is not used in high-energy physics applications, such as elementary particle colliders.

Hybrid pixel detector

Hybrid pixel detector construction and electronic chip inside the detector are made to reduce the loss effect of converting from x-ray photons to electrons. This detector is used in applications that require accurate positioning and short response time. As in the case of the CERN accelerator, the speed of sensor response to collision radiation is one of the most important requirements in elementary particle collision applications. Since its response time is only a few nanoseconds, this type of detector is more complex than maps. In addition, this detector can be created in different sizes and synchronize the entire group, to take the temporal and spatial information very accurately in a time that does not exceed a few nanoseconds [18]. (See Fig. 4) 3D design Hybrid pixel detector sensor.

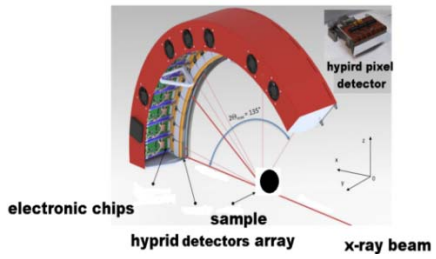

Fig. 5. 3D design Hybrid pixel detector.

In this Fig at general the hypird x-ray detectors system consist of An array of sensors in a circular shape, followed by electronic amplifiers, which amplify the electrical signal resulting from the process of converting the X-rays falling on the sensor into electrical signals, containing information about the interaction of the X-rays with the sample to be tested. There are several types of this sensor, the most important of which is in Table. 1. Where it also explains the most important technical specifications of these different types [19].

Table. 1. Several types of Hybrid pixel detectors

Specification	PILATUS 100 k	PILATUS 300k	PILATUS 1M	XPAD
Area	83.8 × 33.5 mm^2	83.8 × 106.5 mm^2	169 × 179 mm^2	75 × 120 mm^2
Number of pixels	487 × 195	487 × 619	981 × 1043	560 × 960
Number of modules	1	3 (1 × 3)	10 (2 × 5)	8 (1 × 8)
Intermodule None gap	None one module	5.5%	8.4%	none tilting
Frame rate	300 Hz	200 Hz	30 Hz	240 Hz
Weight	~ 4 kg	~ 10 kg	~ 25 kg	~ 15 kg

The XPAD3 X-Ray Camera

This type of X-ray detector camera is the most accurate. It was developed in the last two decades, and it is noted that it provides a high-resolution image, given that the number of pixels has 9600. The IBM 0.25µm deep sub-micron technology was used in the design of the XPAD3 chip. The sole difference between the two versions of the chip (XPAD3-S and XPAD3-C) is in the pixel layout. Table 2 lists the main characteristics of the XPAD3-S and XPAD3-C [20]. (See Fig. 6) 3D design of the XPAD3 x-ray camera.

Table. 2. The main characteristics of the XPAD3-S and XPAD3-C

Specification	XPAD3-S	XPAD3-C
Number of pixels	9600	9600
Pixel size	130 × 130 μm^2	130 × 130 μm^2
Counting rate	≤ 10^6 photons/pixel/second	≤ 10^6 photons/pixel/second
Chip readout	< 1 ms	< 1 ms
Counter depth	12 bits + overflow	12 bits + overflow
Power	< 70 µ W/pixel	< 70 µ W/pixel
Input polarity	Holes collection	Electrons collection
Selection mode	Single threshold	Double threshold
Nonlinearity	< 10% over 35 keV	< 10% over 60 keV
Electronic noise (rms)	< 130 e−	< 130 e−
Threshold dispersion	~ 50 e−	~ 50 e−

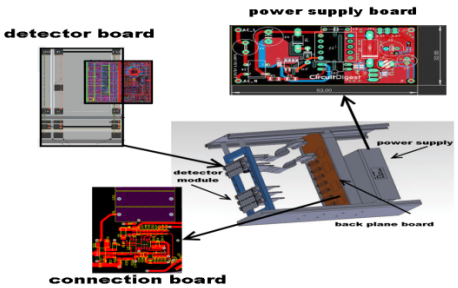

Fig .6. General configuration 3D design of the XPAD3 X-ray camera.

In this Figure, the general installation of the XPAD3 X-ray camera detection system is shown. The system consists of three main parts. First, the array of detectors, which are semi-conductor chips that convert the X-rays falling on them from the sample into electrons in the case of XPAD3-C, or holes as in the case of XPAD3-S. Secondly, the part of the connection board and data transmission, which is a board connected to the part of the signal amplification board after the conversion from X-rays to electrons. Thirdly, it is the main supply source for the previous two parts, and it is

necessary that the supply system gives very smoothing continuous voltage values, due to the sensitivity of the detectors, which also, the system as a whole is equipped with an internal cooling system that reduces the impact, noise resulting from the air temperature, and working together. So as not to affect the sensitivity of the detection system as a whole.

Optical Proposed System Design

In this section, we will explain the design of the proposed X-ray optical system. As the important thing in the application of detecting defects in solid rocket fuel is the quality of the captured image, with the lowest sensitivity of the detection system, which facilitates the image processing process. And take less time in the process of analysing the image to take the results.

The proposed system consists of three main sections. First, the X-ray generation system, which is a valve consisting of a cathode for the production of electrons and an anode, the target material that produces X-rays, and a ceramic valve that contains the components of the X-ray generation device. As for the external components, it is a feeding source for the cathode and it produces a low voltage. With a high current value at a negative value in order to produce electrons on the surface of the filament. Since the ceramic valve is empty of air, this makes the generated electrons free to move and leave the surface of the filament.

The main external component on which the generation of X-rays depends is the high voltage power supply. According to the value that it produces, the spectrum generated for X-rays is determined by hard or soft [21].

Secondly, the X-ray optical system, which is a system that focuses the X-rays, so that all the rays produced from a valve are directed completely at the sample to be examined, which gives a higher image quality. Optical systems in X-rays depend on the theory of reflection of coated surfaces. With the element gold and iridium, because of their good reflective properties when X-rays fall on them and below we will provide a detailed explanation of them in terms of design and manufacturing [22].

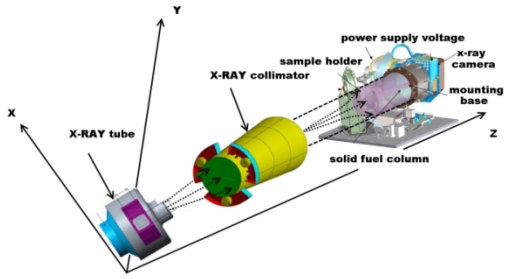

Fig.7. The general block diagram of a proposed optical X-RAY system.

Third, the proposed detection system is an X-ray camera and the optical system assigned to it. In the above, the types of modern X-ray detectors were mentioned, which were developed in the last two decades from 2000 to 2022.One of the most important factors for choosing an x-ray camera is the coefficient of accuracy and clarity of the image, that is, at the pixel level in terms of its area, the speed of the camera's response, and the intensity of its sensitivity. Below, a careful analysis of the selected camera specifications will be made, along with the optical system assigned to it in detail [23]. (see Fig.7) The general block diagram of a proposed optical X-RAY system.

X-RAY Tube Design AND Analysis

In this section, will deal with the detailed design of the x-ray in terms of the external design, using the CAD programs. (See Fig. 8) shows the 3D design of x-ray tube from outside and inside with dimensions. The Figure presents a three-dimensional design of the x-ray tube, where 6 longitudinal and cross-sections are shown in dimensions, and the names of the main parts of the x-ray tube are identified on them.

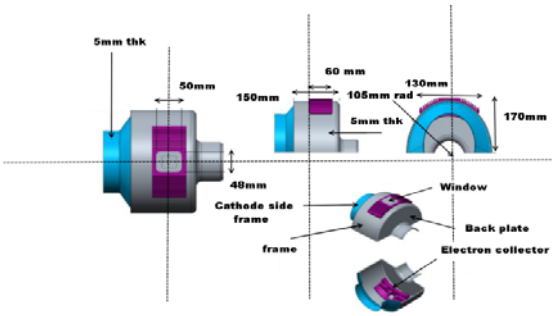

Fig.8. 3D design of x-ray tube from outside and inside with dimensions.

The X-ray tube consists of a metal tube, with a window made of beryllium, an electron collector of copper, a frame made of stainless steel 304L, a back plate and a cathode side frame made of the same metal. Therefore, we had to make an analytical study in the science of materials used in manufacturing the tube x ray. Because it allows the creation of innovative materials and serves as a foundation of knowledge in materials engineering, materials analysis is essential for the development of materials science for manufacturing. Engineers must be aware of the optimal analytical method for these materials and the effect of stress, pressure and temperature. With this knowledge, they are able to identify the limitations of existing materials and how they change with use, develop new materials with desirable properties, and use existing materials in a variety of applications. They can also choose the best materials for a particular application based on performance and cost.

Therefore, a careful analysis was carried out in the ANSYS program to determine the quality of those materials used to manufacture the X-ray tube. (see Fig. 9) the results thermal analysis. Analysis summary shows that in a conceptual design, the window temperature rises, in which the collector temperature follows a direct relationship, at the same time that the anode attracts a dispersed electron that strikes the back plate and frame. This system may reach the point of thermal breakdown, resulting in anode corrosion and window damage, which forces us to consider the operating time and voltage required for the safe operation of the system. These analyses were performed assuming that the time is 50 sec and the applied voltage is 150 kV.

(see Fig.10) the external chassis, with the inlet and outlet of the cooling system from different sides by solid works program, necessary for operation, as the temperature resulting from the collision of electrons with the target material is high, which affects the physical properties of the tube wall, and also affects the rest of the components negatively with the number of operating hours.

In this Figure, a simulation was made by using the ANSYS program to find out the extent of the effect of temperature and pressure on the wall of t a proposed tube producing x-rays, and the simulation was divided into three stages as shown in the Figure, the starting stage, the efforts required to work between the cathode and the anode are shed, which are 150 kilovolts. The single cathode operating voltage is -15 volts, 20 amps. It is noted that the temperature rises from 60 to 240 K, when the cooling system is working. As for the second stage, which is the stage of sustaining work at a time of 50 seconds, it is noted that the temperature rises from 212 to 280 K. With the

generation of spots with a higher thermal nature than the others, the thermal balance of the tube body remains homogeneous. The third and final stage in thermal analysis is the specific stage for critical temperature points. They are the points that can, with the continuity of the work, induce a harmful effect on the body of the pipe, which is limited to the operating time. From this study, we can determine the flow rate of the refrigeration cycle and its effect on the pipe body to mitigate the effects resulting from the work heat.

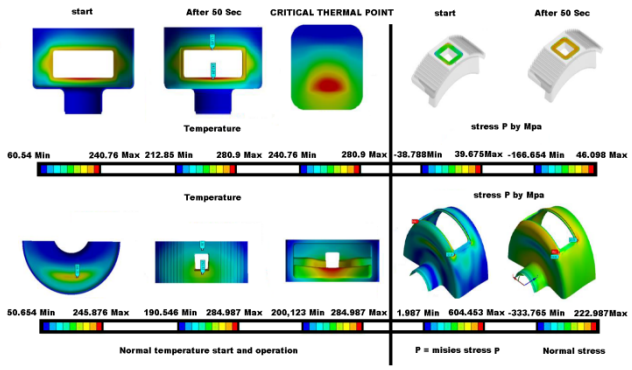

Fig.9. The results thermal and stress analysis by ANSYS.

The second part of the Fig is dedicated to the effect of pressure on the pipe wall in operating conditions. At the start of operation, the system is affected by a pressure of -38 to 40 Mpa. This is a normal and homogeneous effect of pressure. Because the tube is deflated at 0.001 pa. When operating, the temperature of the tube body rises, which induces expansion in the tube body, thus changing its dimensions and pressure. And when 50 seconds pass, there are some points that have pressure higher than the other, and this is a result of the expansion associated with the temperature of those points.

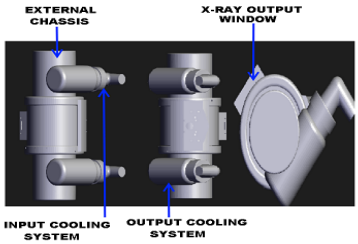

Fig.10. Shows the external chassis, with the inlet and outlet of the cooling system from different sides.

(See Figure 11) the outer final shape of the X-ray tube, showing the shape of the window, from which the X-rays exited, and the entrance and exit of the cooling. This chassis was made of antimony. Covered from the inside with a frame of lead. To enhance protection from X-ray scattering in all directions. And until the x-rays come out of the window only.

Fig .11. The outer final shape of the X-ray tube.

X-RAY Collimator Design and Analysis

In this part, the proposed design of the X-ray system will be discussed. In order to focus on the sample to be photographed from the inside of the solid rocket fuel. It is typical to utilize a combination of a few different materials to shield or collimate x-ray rays. The secondary x-rays that are created as a result of the interaction between the main x-rays and the collimator material can be reduced or absorbed by the use of various materials. For this reason, a primary collimator was constructed using a combination of four different substances: lead, tin, copper, and aluminium, in that order. The primary collimator was constructed primarily out of lead (Pb). One of the least expensive high Z materials, lead is frequently utilized for collimating or shielding various ionizing radiations. Lead has greater x-ray attenuation coefficients (photon absorption cross-sections) compared to other solid materials including copper, iron, and copper. Lead has a higher mass attenuation coefficient than lower Z materials, increasing the likelihood of incident x-rays interacting with lead atoms. Given that x-rays may penetrate any substance, whether its primary or the solid aperture edge of the collimator should emit secondary x-rays, which, as depicted (see Fig. 12), can pollute the collimated beam. In the outskirts the x-rays can be I some of the primary photons of the collimated beam that do not undergoing any interaction as they pass through the collimator's solid perimeter. Aperture, distinguishing X-rays that match Lead's absorption lines, the photons produced by the photoelectric effect. To define Material depth required, according to equation 2, to reduce the X-ray intensity, the dispersant, which passes through the collimator [24].

(2) $$X = \frac{ln\left(\frac{I_o}{I}\right)}{\mu(cm^{-1})} = \frac{ln\,100}{\mu(cm^{-1})}$$

Where I_0 the intensity of x-ray before pathing through collimator, I the intensity of x-ray after pathing through collimator, μ and total mass attenuation coefficients. When μ = $0.4757cm^{-1}$ note this value is a minimum value of mass attenuation, X = 9.68 cm nearly 10 cm. below is the substitution with the equation.

(3) $$X = \frac{ln\left(\frac{I_o}{I}\right)}{\mu(cm^{-1})} = \frac{ln\left(\frac{100}{1}\right)}{0.4757cm^{-1}} = 9.68cm$$

The primary collimator was made of 10 cm thick lead. A coating of tin was placed next to the lead to absorb the characteristic x-rays and photons of 511 KeV, which resulted from the photoelectric phenomenon as a result of the interaction of the x-rays with lead atoms.

The mass attenuation coefficients on tin for the 511 keV photons and the distinctive x-rays from lead, as reported in Table. 3., were used to determine the thickness of tin that was necessary. The mass attenuation coefficient for the 511 keV photon mentioned in Table 3 has a minimum value of 0.09 CM^2/gm, or $0.67CM^{-1}$. Tin's thickness next to lead was determined to be the 100th value layer for 511KeV [25]. From Equation 2, the depth of the tin can be calculated.

(4) $X = \frac{ln\left(\frac{I_o}{I}\right)}{\mu(cm^{-1})} = \frac{ln\left(\frac{100}{1}\right)}{0.67cm^{-1}} = 6.84cm$ Nearly 7cm

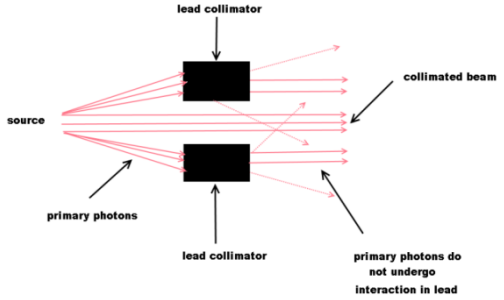

Fig.12. Divergence of x- ray by using a lead collimator.

Table. 3. Lists the total μ for photons whose energy falls within the lead-on-tin absorption range.

Lead Absorption Lines	Energy by KeV	Lead On tin, the overall absorption coefficient μ
M5	2.48	980.20
M˙4	2.59	880.90
M3	3.07	579.30
M2	3.55	401.80
M1	3.85	327.70
L3	13.04	67.81
L2	15.20	45.00
L1	15.86	40.10
K	88.00	2.35

There will be some tin-specific x-rays produced as a result of including the 7 cm tin layer. Copper was applied as a coating to absorb the distinctive x-rays of tin. Consideration was given to the energy of the primary characteristic x-rays from tin described in Table. 4. When determining the needed thickness of the copper layer [26].

Table. 4. Characteristic photons from tin on copper and their μ.

Absorption Lines of Tin	Energy keV	Total absorption coefficient on Copperμ
L3	3.93	364.40
L2	4.16	313.10
L1	4.46	257.90
K	29.20	11.77

Table. 4 show that the K line on tin has a minimum value of 11.77 $cm^{2/g}$ or 105.46 cm^2 on copper. This number was used to find the depth of the copper layer as follows.

(5) $X = \frac{ln\left(\frac{I_o}{I}\right)}{\mu(cm^{-1})} = \frac{ln\left(\frac{100}{1}\right)}{105.46cm^{-1}} = 0.043$cm Nearly 0.5mm

To effectively absorb the x-rays that the tin emits, a 1.5 mm layer of copper was placed beneath the tin. Finally, a layer of aluminium was placed below copper to absorb the distinctive x-rays emitted by copper.

A coating of aluminium that is the necessary thickness

Designed with consideration for the activities of copper and its unique X-ray energy, Table. 5. Displays the absorption coefficients for aluminium [27]. Calculate the thickness of those aluminium.

(6) $X = \frac{ln\left(\frac{I_o}{I}\right)}{\mu(cm^{-1})} = \frac{ln\left(\frac{100}{1}\right)}{96.99cm^{-1}} = 0.047\ cm$ Nearly 0.5mm

Table. 5. Shows the mass attenuation coefficients for the characteristic copper photons on aluminium.

Absorption Lines of Copper	Energy keV	Total absorption coefficient on Aluminium
L1	1.10	927.90
K	8.98	35.94

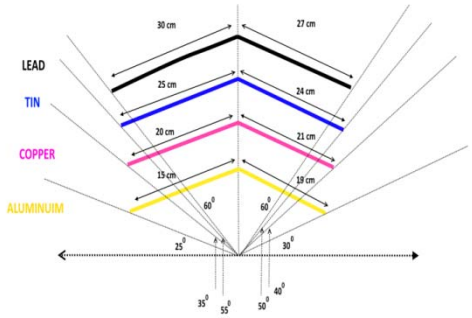

Fig.13. Dimensions and angles of a proposed collimator.

In the upper part of that part, the thickness of the elements used in the manufacture of the collimator was calculated. The geometric shape of the collimator remains. It was manufactured in a semi-conical shape in order to ensure gathering the x-ray photons, and fall on the sample directly to ensure penetration and good interaction with the sample, to form an image accurate as shown (see Fig. 13) .Four layers of metals were used in this collimator, which are lead, tin, copper and aluminium, as shown in the Figure. (See Fig .14) 3D design of a proposed collimator after ray tracing and external bearing chassis.

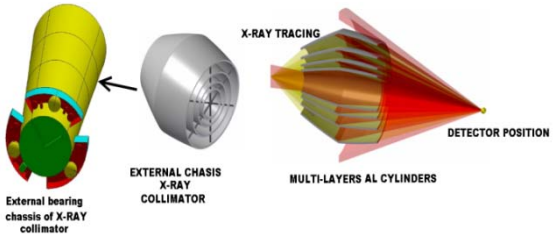

Fig.14. 3D design of x-ray collimator and x-ray tracing internally.

(see Fig. 15) the real picture of the collimator, after manufacturing, but it is noted that the different layers of materials used in manufacturing were divided, in order to notice the presence of distinct X-rays that the X-ray detector senses inside the test chamber, and therefore it was divided into 25 slices with the same design dimensions, but with slices farther from Some are 3 mm. This is to ensure that the rays are completely collected within the proposed system. And then make a high concentration of rays to provide a high-resolution image. The blue light in the picture is a light source to show the difference between the layers from which the collimator was made.

In Part No. 3, the most important modern X-ray detectors are listed, especially XPAD-3-C, which is one of the latest cameras used in monitoring X-rays as their specifications were listed, so they were selected as the proposed detection system for solid rocket fuel samples. In the following, everything related to the design of the detector for the proposed system will be discussed step by step. Hybrid pixel area detectors, sometimes known as "pixel detectors", are a new generation of X-ray detectors that rely on single photon counting and direct detection. High and wide linear range an unparalleled level of noise is achieved through dynamic and extremely low noise. Fast readout time and good signal-to-noise ratio (high frame rates) one of its inherent qualities that contribute to its appeal is the electronic shutter. These reagents are initially being used on synchrotron beam lines and are showing promise in the lab. A full XPAD frame is obtained after reading four ASCII files, one for each unit.

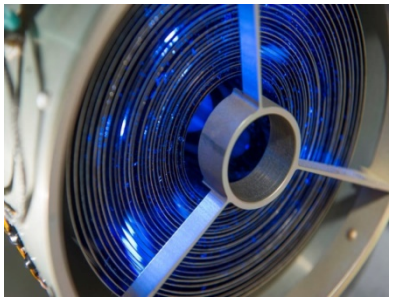

Fig.15. Real image inside x-ray collimator.

X-Ray Camera of Proposed System Design

The parallel electrical engineering and processing of this detector results in an acquisition time of 2 ms per image (500 Hz frame rate). No matter the detector size, the frame rate exceeds 700 Hz with the latest XPAD detectors. The limitations of a pixel detector are the same as those of a

single pixel point detector because a pixel detector is an array of hundreds of thousands of independent point detectors running in parallel. Dynamic range is 28 bits (12 bits for high frame rate mode, 32 bits for more modern XPAD detectors). The dead time related to the maximum count rate is 250 000 photons per second. (See Fig.16) shows the 3d design of proposed camera.

The x-ray camera from inside consist of patch panel, patch panel transceiver, patch panel flex cable, safety inter lock board, input and output board, vacuum line and module of inter connection board. In camera chassis outside , It is noticed that there is a cylindrical part from the back, which is the nitrogen cooling system, where the cooling degree reaches 42 below zero, and this is to ensure that the camera works with high quality.(see Fig .17) the real image of X-ray camera [28].

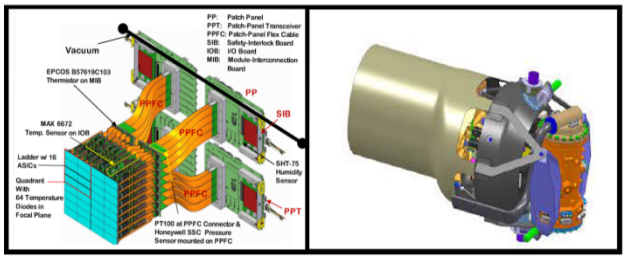

Fig.16. The 3d design of proposed camera.

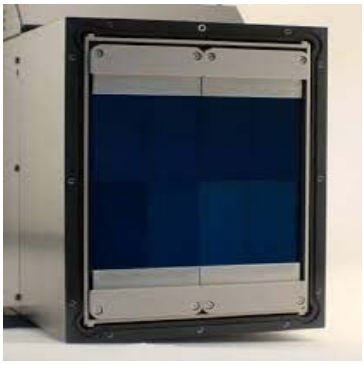

Fig .17. The real image of X-ray camera.

The mechanical equipment in which the camera is installed, in addition to the solid rocket fuel sample, as shown in the three-dimensional (see Fig. 18) it consists of 12 aluminium columns, which are the main component of the mechanical equipment, and a number of flanges. Two of them are to install the solid rocket fuel sample, and the other to install the X-ray receiving camera after the sample is penetrated. (See Fig. 19) the real image of mechanical equipment after implementation. Dimensions of this mechanical equipment, the total length are 1.5 meters, the diameter of the flange is 30 cm, and that is for the first and the last. As for the medium flange, it has a diameter of 35 cm.

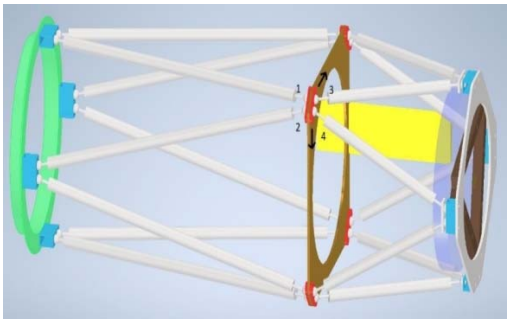

Fig. 18. 3D design of mechanical equipment of proposed system.

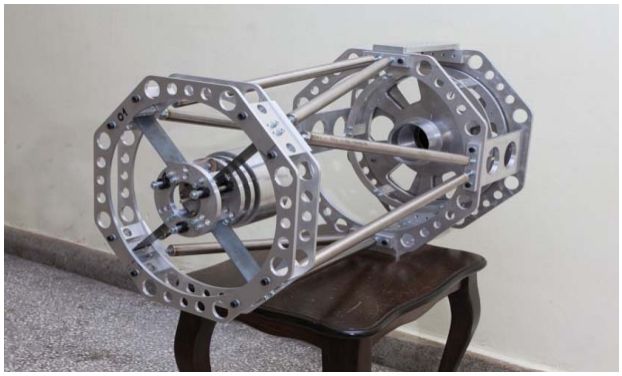

Fig.19. Real image of a mechanical equipment of proposed system.

X-Ray Camera Hardware Design

The processing system of the X-ray sensor camera is divided into four signal processors, one is master and three are slaves, so that the main signal processor can collect their parameters and process them in parallel to produce the image with a delay time of 2 ms.

The external components of each signal processor are, XFEL signal, power supply, ETHERNET, JTAG programmer, WAMING LEDS, LP2468 microcontroller piggy in Figure 20 shows the slave signal processing board. The complete signal processing board (SIB) configuration of the mega pixel camera is shown in (see Fig. 20), along with a comprehensive description of the device. The only difference between the master and the SIB server is that the SIB master has the additional ability to monitor signals from external interfaces.

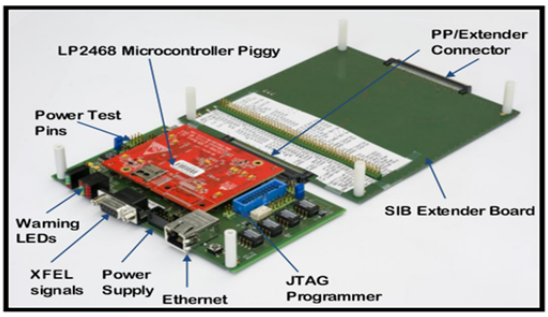

Fig. 20. Signal processing board slave external comments.

Through the Q-Loop, the four SIBs can communicate with each other. Each SIB collects data from four MAX6672 temperature sensors on the IOB, four EPCOS-B57619 thermometers on the MIB, four Honeywell SCMNNN1 pressure sensors on the PPFC, and four Pt100 temperature sensors placed on the PPFC. On the cold trap a different Pt100 temperature sensor is placed (not shown). The lowest reagent room temperature was found in this cold trap instrument [29].

The main signal processing board is, FPGA Startixll GX. It supports the x1, x4, and x8 PCI Express protocol setups. Eight gigabits of sending and receiving bandwidth are provided by the high-speed connector that connects the optical transceivers to the board. 2.5 GHz). The XpressLite2 PCI Express endpoint with DMA25 is included with the XpressGXII development board. Two optical fibers connect the board, which is hooked into the PC, to the detector acquisition system. On a daughter mezzanine board that is connected to the high speed interface, the optical transceivers are mounted. (See Fig. 21) shows the master signal processing board with the optical interface [30].

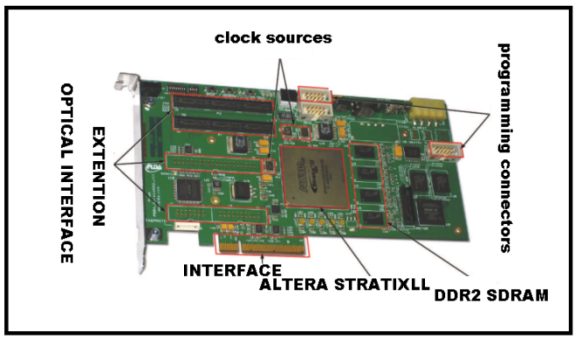

Fig. 21. The master signal processing board with the optical interface.

RESULTS

In the experiments that we have done, on solid rocket fuel columns186mm and x-ray voltage 170 KV. The first tests were conducted on two samples of the initial missile fuel, a healthy sample that did not have any manufacturing defects, and the second when pouring the fuel column, air bubbles were intentionally present to ensure that the proposed system detected these air bubbles and determined their exact location. (see Fig. 22) shows the defect-free sample (A), and the sample with air bubbles (B).

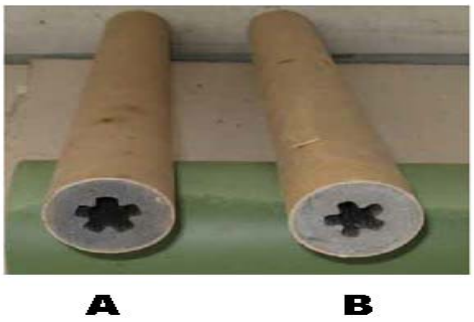

Fig. 22. The defect-free sample (A), and the sample with air bubbles (B).

Pictures of the two samples were taken using the proposed system, with an illustrative histogram for them to show the accuracy in taking pictures taken for the samples. In (see Fig. 23), it shows the image of the sample without defects after imaging, with careful processing of the image with the XPAD-3-C camera program.

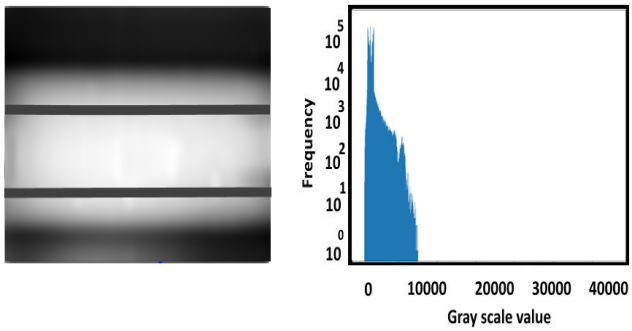

Fig. 23. The image of the sample without defects.

In this Figure, it is clear that the rocket fuel column has no air bubbles, i.e. it was well made and completely deflated from air. And the histogram image shows a continuous, uninterrupted density, which indicates that the image does not have an inconsistent density distribution, which proves that the sample to be tested was made as desired. (see Fig. 24), the image of the rocket fuel sample is shown after careful processing using the X-ray camera program to clarify the smallest details whether there are bubbles or not and whether these bubbles contain impurities from manufacturing or not, because this directly affects the process of stabilizing the combustion rate, which affects I have to balance the missile in the air. It is noticed that there is a slight air bubble in the right part of the image, which does not affect the stability of the combustion rate. Because it is in the aperture of the missile fuel column, not from the inside.

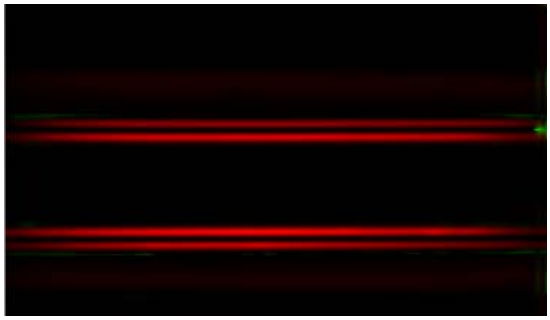

Fig. 24. The image of the rocket fuel sample is shown after careful processing by x-ray camera program.

(See Fig. 25) shows the solid missile column No. B. This column has serious manufacturing defects, as there are several air bubbles on the inside, and the histogram distribution of the image is not homogeneous by nature, as a result of the presence of these air bubbles. Perspective pointing with the arrow was made on the location of one of the bubbles, as shown in this Figure.

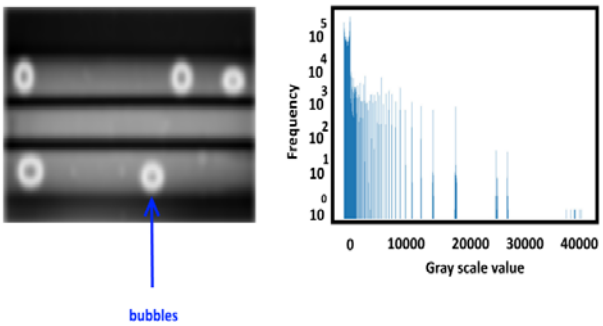

Fig. 25. The image of the sample with defects.

(See Fig. 26) it shows the image of the sample after processing an accurate indication of it to indicate whether the air bubbles contain impurities from the compounds manufactured for the missile fuel column or not. And you notice the presence of some impurities in those bubbles shown in green in that Figure. It is clear to us that the proposed system does not only determine the locations of the air bubbles, but it can also determine whether there are impurities from the manufacturing compounds inside these bubbles or not.

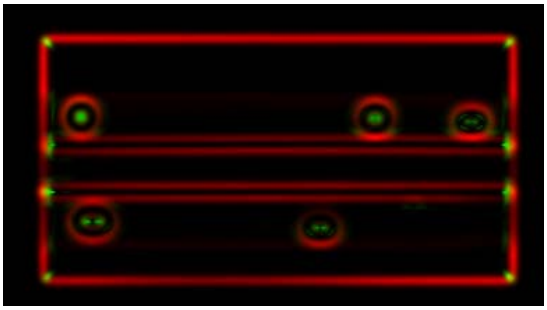

Fig. 26. The image of the sample after processing by x-ray camera program.

Conclusion

The proposed system was designed and implemented according to the latest techniques of visual diagnostic x-ray in the field of non-destructive testing. The proposed system succeeded remarkably in providing accurate images of solid rocket fuel samples that were tested. It is worth noting that the proposed collimator system, which was implemented, succeeded well in collecting X-rays and focusing them on the sample. Which significantly helped in forming a very good image on a camera for receiving x-rays. The X-PAD-3-C camera was chosen to work in that proposed system. It is worth mentioning that it is one of the latest x-ray detection techniques, as it provides an image at a rate of 2 mm per second. It is also characterized by a powerful and very sensitive image processor, which gives accuracy in the details of the image taken for the sample of solid rocket fuel. The proposed system was tested on two real rocket fuel samples to ensure the quality of the image captured through it. The system has proven to be effective in evaluating the performance of solid rocket fuel manufacturing without the need for costly and dangerous field tests at the same time.

DECLARATION OF COMPETING INTEREST

The authors declare that they have no known competing financial interests or personal relationships that could have appeared to influence the work reported in this paper.

ACKNOWLEDGMENTS

The authors are very grateful to the members of the Communication and Electronics Engineering branch, Faculty of Engineering, Aswan University, Aswan, Egypt for their encouragement, support, and help.

REFERENCES

[1] L. F. Nascimento. Brief history of X-ray tube patents. *World Patent Information* (2014), 37, 48-53.

[2] N. N. Azman, S. Siddiqui, R. Hart, and I.-M. Low. Effect of particle size, filler loadings and x-ray tube voltage on the transmitted x-ray transmission in tungsten oxide—epoxy composites. *Applied radiation and isotopes* (2013), 71, 62-67.

[3] M. Dehairs, H. Bosmans, and N. Marshall. A study of the impact of x-ray tube performance on angiography system imaging efficiency. *Physics in Medicine & Biology* (2020), 65, 225028.

[4] B. W. Pogue and B. C. Wilson. Optical and x-ray technology synergies enabling diagnostic and therapeutic applications in medicine. *Journal of biomedical optics* (2018), 23, 121610-121610.

[5] H. Wei, Y. Fang, P. Mulligan, W. Chuirazzi, H.-H. Fang, C. Wang, et al. Sensitive X-ray detectors made of methylammonium lead tribromide perovskite single crystals. *Nature Photonics* (2016), 10, 333-339.

[6] T. Marshall, J. Evans, and R. Frederick. UAH Solid Propellant Characterization. *in 43rd AIAA/ASME/SAE/ASEE Joint Propulsion Conference & Exhibit* (2007), 5763.

[7] A. M. Toscana, M. R. Lato, D. Fontanarosa, and M. G. De Giorgi. Optical Diagnostics for Solid Rocket Plumes Characterization: A Review. *Energies* (2022), 15, 1470.

[8] A. Yu. Krainov, V. A. Poryazov, and D. A. Krainov. Mathematical modelling on extinction of metallized composite solid propellant under a sudden drop in pressure. Propellants, Explosives, *Pyrotechnics* (2022), 47, e202100123.

[9] Z. Wang, H. Xie, S. Xiang, K. Ouyang, L. Bao, R. Shen, et al. Multi-stage combustion characteristics of sodium perchlorate/lithium perchlorate-based electrically controlled solid propellant. *Chemical Engineering Journal* (2023), 456, 140958.

[10] L. Jie-Yao, Y. Su-Lan, W. Shixi, T. Gen, Y. Wenming, and Y. Qi-Long. Burning rate modulation for composite propellants by interfacial control of Al@ AP with precise catalysis of CuO. *Combustion and Flame* (2022), 240, 112029.

[11] H. Tian, Z. Wang, Z. Guo, R. Yu, G. Cai, and Y. Zhang. Effect of metal and metalloid solid-fuel additives on performance and nozzle ablation in a hydroxy-terminated polybutadiene based hybrid rocket motor. *Aerospace Science and Technology* (2022), 123, 107493.

[12] W. Pang, V. Abrukov, D. Anufrieva, and D. Chen. Burning Rate Prediction of Solid Rocket Propellant (SRP) with High-Energy Materials Genome (HEMG). *Crystals* (2023), 13, 237.

[13] L. Li, J. Ren, P. Wang, Z. Lü, X. Li, and M. Sun. An adaptive false-color enhancement algorithm for super-8-bit high grayscale X-ray defect image of solid rocket engine shell. *Mechanical Systems and Signal Processing* (2022), 179, 109398.

[14] L. Li, J. Ren, P. Wang, H. Gao, M. Sun, B. Sha, et al. A pixel-level weak supervision segmentation method for typical defect images in X-ray inspection of solid rocket motors combustion chamber. *Measurement* (2023), 112497.

[15] L. Xue, J. Hei, Y. Wang, Q. Li, Y. Lu, and W. Liu. A high efficiency deep learning method for the x-ray image defect detection of casting parts. *Measurement Science and Technology* (2022), 33, 095015.

[16] P. Maken and A. Gupta. 2D-to-3D: A Review for Computational 3D Image Reconstruction from x-ray Images. *Archives of Computational Methods in* Engineering (2023), 30, 85-114.

[17] C. Neubüser, T. Corradino, G.-F. Dalla Betta, S. Mattiazzo, L. Pancheri, and A. Collaboration. First characterization results of ARCADIA FD-MAPS after X-ray irradiation. *Journal of Instrumentation* (2023), 18, C01066.

[18] P. Skrzypiec and R. Szczygieł. Readout chip with RISC-V microprocessor for hybrid pixel detectors. *Journal of Instrumentation* (2023), 18, C01030.

[19] J. Quercia, F. Mele, D. Macera, B. Arcaini, B. Garavelli, and G. Bertuccio. Experimental characterization of a fast X-ray spectroscopic imager module using the ALTAIR P3 ASIC for real-time contaminants detection. *Journal of Instrumentation* (2023), 18, C01064.

[20] H. O. Dávila, S. Martinez-Ovalle, and H. Vega-Carrillo. Study of X-ray scattered in a phantom as function of its maximum energy during bimodal PET/CT imaging. *Applied Radiation and* Isotopes (2019), 148, 1-6.

[21] B.-B. Zhang, E.-W. Liang, and B. Zhang. A comprehensive analysis of Swift XRT data. I. Apparent spectral evolution of gamma-ray burst X-ray tails. *The Astrophysical Journal* (2007), 666, 1002.

[22] D. Gamdha, S. Unnikrishnakurup, K. J. Rose, M. Surekha, P. Purushothaman, B. Ghose, et al. Automated defect recognition on X-ray radiographs of solid propellant using deep learning based on convolutional neural networks. *Journal of Nondestructive Evaluation* (2021), 40, 1-13.

[23] L. Li, J. Ren, P. Wang, H. Gao, M. Sun, B. Sha, et al. A pixel-level weak supervision segmentation method for typical defect images in X-ray inspection of solid rocket motors combustion chamber. *Measurement* (2023), 112497.

[24] S. M. P. Kalaiselvi, E. Tang, H. Moser, M. Breese, S. P. Turaga, H. Kasi, et al. Wafer scale manufacturing of high precision micro-optical components through X-ray lithography yielding 1800 Gray Levels in a fingertip sized chip. *Scientific reports* (2022), 12, 1-12.

[25] M. Hossein, S. M. Reza, and S.-N. Jamshid. Image quality and dose assessment of collimator slit width effect in SLOT-SCAN X-ray imaging system. *Applied Radiation and Isotopes* (2021), 171, 109642.

[26] B. Whelan, S. Trovati, J. Wang, R. Fahrig, P. G. Maxim, A. Hanuka, et al. Bayesian optimization to design a novel x-ray shaping device. *Medical Physics* (2022), 49, 7623-7637.

[27] S. Stoupin, A. MacPhee, N. Ose, M. MacDonald, L. Masse, D. Rusby, et al. A Monte Carlo technique to model performance of streak camera-based time-resolving x-ray spectrometers. *Review of Scientific Instruments* (2022), 93, 093510.

[28] E. Kalemci, O. Turhan, İ. Kuvvetli, S. Schanne, M. Hernanz, P. Orleański, et al. The instrument control unit processing hardware and software of the wide field monitor on eXTP. *in Space Telescopes and Instrumentation: Ultraviolet to Gamma Ray* (2022), 1592-1604.

[29] J. Reiffers, S. Albrecht, O. Hälker, A. Lederhuber, B. Mican, and F. J. Veredas. Hardware development of Athena WFI frame processing module. *in Space Telescopes and Instrumentation: Ultraviolet to Gamma* Ray (2022), 948-958.

[30] M. Edwards. Designing a Hybrid Digital/Analog Quantum Physics Emulator as Open Hardware. *arXiv preprint arXiv* (2023), 2302.00821.